Electronic Supplementary Material (ESI) for Catalysis Science & Technology.

Supporting Information

Reductant composition influences the coordination of atomically dispersed Rh on anatase TiO_2

Chithra Asokan [1, †], *Ho Viet Thang* [2,3 †], *Gianfranco Pacchioni* [2,*], *Phillip Christopher* [1,*]

[1]Department of Chemical Engineering, University of California Santa Barbara, Santa Barbara, California 93106, USA.

[2] Dipartimento di Scienza dei Materiali, Università di Milano-Bicocca, via Cozzi 55, 20125 Milano, Italy.

[3] The University of Da-Nang, University of Science and Technology, 54 Nguyen Luong Bang, Da-Nang 550000, Vietnam

Corresponding author: pchristopher@ucsb.edu, gianfranco.pacchioni@unimib.it

[†] These authors contributed equally to this work

TABLE OF CONTENTS

Supplementary figures and tables:

Experimental methods

Synthesis

Atomically dispersed Rh on anatase TiO_2 was synthesized by utilizing strong electrostatic adsorption (SEA) principles a Rh weight loading of 0.1 wt%. High surface area anatase TiO_2 support (US Nano # US3838, 5 nm diameter, 99.9% purity) and the Rh precursor (Sigma Aldrich # 206261, Rh(III) chloride hydrate) were diluted in water separately with total liquid volumes of the two solutions at a 4:1 ratio, which gives a support surface loading of 2900 m^2/L based on a measured TiO_2 surface area of 290 m^2/g. NH_4OH was added to the separate support and precursor solutions to target a pH of 9. The precursor solution was injected at a rate of 4 ml/min into the support solution while constantly stirring at a high rate of 350 rpm. Then, the solution was heated to 70 °C until water evaporated, and the sample was dried completely. The sample was kept overnight in a 100 °C oven and then ex-situ calcined in 10% O_2 /He for 4 hours at 350 °C.

Probe CO FTIR

The catalyst was loaded in a Harrick Low Temperature Reaction chamber mounted inside a ThermoScientific Praying Mantis diffuse reflectance adapter set in a Nicolet iS10 FTIR spectrometer with a Mercury Cadmium Telluride (MCT) detector and mass flow controllers (Teledyne Hastings) were used to control the gas flow rates across the reactor bed. Catalysts were in-situ pretreated for 30 minutes at 350 °C in pure O_2 and then subsequently in 10% H_2/Ar at 100 °C or in 10% CO/Ar at 300 °C for 1 hr. CO probe molecule IR was executed by decreasing the temperature following pretreatment in Ar to room temperature, exposing the sample to 10% CO in Ar for 10 minutes, purging in Ar for 10 minutes, and then collecting spectra with 12 scans and 0.482 cm^{-1} data spacing. Temperature programed desorption (TPD) measurements were executed by heating in Ar at a rate of 20 °C /min until complete desorption of CO was observed and taking spectra every 20 °C during desorption. The rate of loss of CO band intensity (corresponding to CO desorption) were calculated using the change in peak areas of deconvoluted (integrated and fit using Origin®) over 40 °C. Probe molecule CO and TPD experiments were also done for samples in-situ pretreated for 30 minutes at 350 C° in pure O_2 and then subsequently in 10% H_2/Ar at 200 °C and 300 °C for 1 hr.

TPD and Redhead Analysis

OriginPro was used to deconvolute overlapping peaks using Lorentzian functions and defining 2 parameters, the peak position and FWHM. In the case where Rh/TiO_2 was reduced at 100 °C in H_2, the deconvolution of the band at 2031 was kept at constant frequency and FWHM. To calculate the rate of change of the bands assigned to Rh(CO) monocarbonyls, 2012 and 1999 cm^{-1} , the area of asymmetric stretch of the $Rh(CO)_2$ species, 2031 cm^{-1} was subtracted from the total normalized integrated area of the 3 peaks. The rate of loss of CO stretch band intensity was calculated by using central finite difference method (equation 1) over 40 °C intervals and was assigned to the desorption of CO from Rh.

$$\left(\frac{d(\frac{A}{A_o})}{dT}\right)_x = \frac{\frac{A_{x+1}}{A_o} - \frac{A_{x-1}}{A_o}}{T_{x+1} - T_{x+1}} \qquad (1)$$

Where:
A= Peak area at temperature T
A_o= Maximum peak area
T= Temperature
x= Point of measurement (at specific T)
$\left(\frac{d(\frac{A}{A_o})}{dT}\right)_x$ = Change in area over change in temperature
T_{x+1}= Temperature at x+1
T_{x+1}= Temperature at x-1
A_{x+1}= Area of peak at temperature T_{x+1}
A_{x-1}= Area of peak at temperature T_{x-1}

To estimate CO binding energy to Rh from experimental data, Redhead analysis[1] was used according to equation 2.

$$\frac{E}{RT_{p=}} ln\left(\frac{vT_p}{\beta}\right) - 3.46 \qquad (2)$$

Where:

E= Energy, kJ/mol
T_p= Temperature at peak desorption rate, K
R= 8.3124 kJ/ K kmol
v = rate constant, $10^{13.6}$ /sec
β = Rate of Temperature, 20 °K/min

Computational methods

DFT Methods

Spin-polarized calculations were carried out with the Perdew-Burke-Ernzerhof (PBE) generalized gradient approximation (GGA) exchange-correlation functional[2] implemented in the Vienna Ab-initio Simulation Package (VASP).[3] The self-interaction error has been partly corrected by applying the DFT+U approach[4,5] in which the Hubbard's U parameter is empirically set to 3 eV for 3d orbital of Ti ions.[6] The core electrons and nuclei interactions are described by projector augmented wave (PAW) method.[7, 8] The valence electrons of Ti (3s, 3p, 3d, 4s), Rh (4p, 4d, 5s), O (2s, 2p), H (1s) and C (2s, 2p) are explicitly considered with plane wave basis set applying a cutoff energy of 400 eV. The calculations were done at the *Gamma* point only and optimized structures were converged when the forces are less than |0.01| eV/Å. described in detail in a previous study.[9] The corresponding formula of TiO_2 (101) and TiO_2 (145) surface models are $Ti_{60}O_{120}$ and $Ti_{88}O_{176}$, respectively. The side view and top view of TiO_2 (101) surface are shown in the Figure S2 where two distinguished Ti sites: 5-fold-coordinated, Ti_{5c} and 6-fold-coordinated, Ti_{6c} and two inequivalent O site, 2-fold-coordinated, O_{2c} and 3-fold-coordinated, O_{3c} are presented. A vacuum by more than 15 Å is created between the slabs to minimize interaction of two neighboring slabs.

The CO adsorption energies, in eV, were obtained by the difference between isolated species and the adsorption complexes. Stable adsorbed species correspond to positive values. The stretching frequencies of CO were calculated within the harmonic approximation, where CO and its first nearest atoms were considered in the calculation. Van der Waals interactions were not included, but it has been shown that for small molecules, such as CO or H_2, the dispersion contribution is minor and does not affect adsorption energies and geometries.[10]

We adopted the models of (3 x 1) and (2 x 1) supercell slabs including five-atomic layers for the anatase TiO_2 (101) and the stepped TiO_2 (145) surfaces, respectively. The bond length and corresponding stretching frequency of gas-phase CO at the PBE level are 1.144 Å and 2125 cm^{-1}, respectively. We applied a scaling factor $\alpha = 2143/2125 = 1.0085$ for all calculated frequencies to take into account the difference with respect to the experimental CO frequency of 2143 cm^{-1}. The effective charge of Rh atoms was analyzed by applying the Bader method.[11, 12, 13, 14] The reaction pathways were searched by using the climbing-image nudged elastic band (CI-NEB) method.[15] Six images were created between reactants and products to find the minimum energy pathway.

Single Rh atom on TiO_2 (101) and stepped TiO_2 (145) surfaces

We adopted six models to describe the nature of a Rh single atom anchored on the TiO_2 surface, Figure S2, including four adsorption species: $(Rh)_{ads}$, $(RhO)_{ads}$, $(RhOH)_{ads}$, $(RhO_2)_{ads}$, and two substitutional positions: a Rh atom substitutional to a lattice Ti, $(Rh)_{subTi}$ and to a lattice O, $(Rh)_{subO}$. In principle two sites, Ti_{5c} and Ti_{6c}, can be replaced by Rh; however, Rh at a Ti_{6c} site is unstable,[16] thus only Rh substitutional to Ti_{5c} site, $(Rh)_{subTi5c}$ was considered. For Rh replacing a lattice O site, we considered only Rh substitutional to O_{2c}, $(Rh)_{subO2c}$. In fact, also Rh at O_{3c} sites is unstable.[14]

The preferred adsorption site on the TiO_2 (101) surface for $(Rh)_{ads}$ is in the center of an hollow site formed by two O_{2c} and two O_{3c} sites, with Rh-O_{2c} bond length of 2.057 and with Rh-O_{3c} bond length of 2.215 Å, Figure S3a. At a stepped site of the TiO_2 (145) surface $(Rh)_{ads}$ is bound to two O_{2c} sites with Rh-O_{2c} distances of 2.129 Å to O_{2c} on the top terrace and of 2.185 Å to O_{2c} at the bottom terrace, Figure S4a.

$(RhO)_{ads}$ units are formed by bonding with an extra O (formally deriving from a surface OH group). Here the Rh atom is bound to two O_{2c} atoms with an identical distance of 2.112 Å on (101) surface (Figure S3b) and of 1.972 and 2.102 Å on stepped (145) surface (Figure S4b).

The presence of OH groups has been observed experimentally. Thus, we also considered $(RhOH)_{ads}$ species on both terrace and step sites of TiO_2. The optimized structures of $(RhOH)_{ads}$ on terrace and step sites of TiO_2 are shown in Figure S3c and Figure S4c, respectively. The Rh-O and O-H distances are 2.30 Å and 0.97 Å (terrace) and 2.00 Å and 0.97 Å (step). The Rh-O bond length of $(RhOH)_{ads}$ species is larger than that on $(RhO)_{ads}$ species on terrace (2.00 Å) and on step site (1.86 Å). This indicates a weaker bonding of Rh with extra the O in $(RhOH)_{ads}$ species compared to that in $(RhO)_{ads}$ species.

$(RhO_2)_{ads}$ units are formally deriving from the interaction with two surface OH groups. Here the Rh atom forms four bonds: two with the two extra O atoms anchored on Ti_{5c} sites, with a distance of 1.831 Å, and the other two with surface O_{2c} and O_{3c} sites with a bond length of 2.129 Å and 2.132 Å, respectively, Figure S3d. Similarly, the $(RhO_2)_{ads}$ unit is anchored at step sites of the (145) surface: two bonds with two extra O atoms with distances of 1.998 and 2.088 Å, and two bonds with two O_{2c} sites with a bond length of 1.827 Å, Figure S4d.

For $(Rh)_{subTi5c}$ species, the substitution of Rh atom at Ti_{5c} does not result in changes in the geometrical parameters of the TiO_2 (101) surface (Figure S3e) and TiO_2 (145) surface (Figure S4e). On the other hand, $(Rh)_{subO2c}$ species are moving up from the original O_{2c} site with elongation of Rh-Ti bonds to 2.453 Å (original O-Ti bond length of 1.889 Å, Figure S3f (TiO_2 (101) surface) and Figure S4f (TiO_2 (145) surface).

The formal oxidation state of Rh, defined by the number of bonds between the Rh atom and the excess O atoms on the surface, is 0, +I, 0, +II for $(Rh)_{ads}$, $(RhO)_{ads}$, $(RhOH)_{ads}$, $(RhO_2)_{ads}$, respectively. For $(Rh)_{subTi5c}$ and $(Rh)_{subO2c}$ species, we assumed the same formal charge of Rh of the lattice Ti and O sites, i.e. +IV and –II, respectively.

Adsorption of a single CO molecule

The adsorption properties of single CO on supported Rh single atom and on bare TiO_2 are reported in Table S1, Figure S4 and Figure S5. On terrace and step site of bare TiO_2 anatase surface CO is weakly absorbed on Ti_{5c} cation sites with an adsorption energy of 0.34 and 0.41 eV, respectively. The corresponding stretching frequencies are 2187 and 2193 cm^{-1} which are blueshifted with respect to free CO by +44 and +50 for terrace and step site, respectively, Table S1. When CO is placed on Rh single atom species, we observed a strong adsorption energy and a large redshift of the CO stretching frequency with respect to gas-phase CO.

On $(Rh)_{ads}$ species, similar characteristics are found for CO adsorbed on Rh located on terrace and on step sites of the TiO_2 surface. Particularly, adsorption energies and stretching frequencies of CO are 2.05 eV, 2017 cm^{-1} for terrace sites and 2.00 eV, 2001 cm^{-1} for step sites, Table S1. The strong adsorption of CO on $(Rh)_{ads}$ species is mainly due to the strong back donation of electrons from the 4d states of Rh to $2\pi*$ state of CO. As a consequence, the CO bond length is elongated from 1.144 Å of free CO to 1.166 Å and 1.168 Å for $CO/(Rh)_{ads}$ on terrace and step sites, respectively.

Considering CO on $(RhO)_{ads}$ species, the adsorption energies are slightly stronger than on $(Rh)_{ads}$ species: 2.24 eV vs. 2.05 eV for terrace sites and 2.45 eV vs. 2.00 eV for step sites, while the CO frequency redshifts are smaller, in absolute values, than those on $(Rh)_{ads}$ species, -84 cm^{-1} vs. -126 cm^{-1} for terrace sites and -90 cm^{-1} vs. -142 cm^{-1} for step sites, Table S1. This is consistent with the lower charge transfer from $(RhO)_{ads}$ species to the $2\pi*$ orbitals of CO compared to $(Rh)_{ads}$ which is confirmed by the Bader charge of Rh: +0.97 |e| vs. +0.64 |e| on terrace sites and +0.92 |e| vs. +0.30 |e| on step sites, Table S1.

We first analyzed the frequency of OH of anatase without CO adsorption. The results are in good agreement with experiment (3730-3789 cm^{-1} vs. 3734 cm^{-1}). Then, we considered the characteristics of $CO/(RhOH)_{ads}$ species, Table S1. Here CO is strongly bound, 2.70 eV (terrace) and 2.90 eV (step), and has a stretching frequency of 2016 cm^{-1} at both terrace and step sites, with a negative shift of 127 cm^{-1} with respect to free CO. This is quite different from the previous case of $(RhO)_{ads}$ due to a formally higher oxidation state of the Rh atom, consistent with a less positive Bader charge, Table S1.

Things are different when we consider CO adsorbed on $(RhO_2)_{ads}$ species on terrace and step sites. While a strong adsorption energy is still observed for CO bound to $(RhO_2)_{ads}$ on terrace, 1.91 eV, the bonding is about 1 eV weaker (1.08 eV) on $(RhO_2)_{ads}$ on step sites. This is due to the difference in adsorption of the RhO_2 unit on terrace and step sites, reflecting the bond-order conservation principle: the binding energy of the RhO_2 unit on step site (1.9 eV) is about 1 eV stronger than that on terrace sites (1.0 eV). However, the Bader charge and redshifts of CO frequency are virtually the same, +1.32 |e| and -44 cm^{-1} for $CO/(RhO_2)_{ads}$ on terrace sites and +1.33 |e| and -52 cm^{-1} for $CO/(RhO_2)_{ads}$ on step sites, Table S1.

On $(Rh)_{subTi5c}$ CO is strongly bound with an adsorption energy of 1.58 eV (terrace) and 1.65 eV (step). Due to the lower charge transfer from Rh to CO only a moderate redshift of CO frequency is found (-23 cm^{-1} for $CO/(Rh)_{subTi5c}$ on terrace, and -26 cm^{-1} for $CO/(Rh)_{subTi5c}$ on step sites, Table S1).

On the last configuration considered, $(Rh)_{subO2c}$, CO is very strongly bound with an adsorption energy of 2.70 eV and 2.56 eV for terrace and step sites, respectively. This is consistent with the largest charge donation from Rh to CO (Bader charge of Rh of -0.02 and -0.11 |e| for terrace and step sites, respectively). As a result, the CO bond length is elongated to 1.170 Å, resulting in the largest redshift of CO stretching frequencies of -146/-150 cm^{-1}, Table S1.

Adsorption of two CO molecules

The adsorption of a second CO (geminal CO complex) was considered for all Rh single atom configurations. In most cases, strong adsorption energies are still observed, except for the case of $(Rh)_{subTi5c}$ where the second CO spontaneously interacts with a lattice oxygen atom forming a

CO_2 species. The properties of geminal CO molecules on $(RhO_x)_{ads}$ species are presented in Table S2.

On $(Rh)_{ads}$ the second CO is bound as strongly as the first CO molecule with an energy of 2.03 eV on terrace and 1.96 eV on step sites, Figure S6a. The two CO molecules on $(Rh)_{ads}$ result in symmetric and antisymmetric stretching frequencies of 2097 and 2026 cm^{-1} (terrace) and 2095 cm^{-1} and 2031 cm^{-1} (step). These values are in very good agreement with IR spectra of geminal CO molecule on isolated Rh species.

When we consider the second CO on the $(RhO)_{ads}$ species, Figure S6b, smaller adsorption energies (about 1eV) were found compared to the first CO molecule, 1.25 eV vs. 2.24 eV (terrace) and 1.08 eV vs. 2.45 eV (step). This is consistent with the smaller charge transfer from Rh to the second CO compared to the first CO molecule, in line with the Bader charge on Rh (+1.02 vs. +0.70 on terrace and +0.97 vs. +0.68 on step). The symmetric and antisymmetric frequencies of geminal CO molecules on terrace sites (2117, 2059 cm^{-1}) are similar to those on step sites (2108, 2057 cm^{-1}), Table S2. Also $(RhO)_{ads}$ species have CO stretching frequencies close to the experimental one, although not as good as the one obtained for $(Rh)_{ads}$.

We also considered the possible reactivity of the second CO adsorbed molecule with an extra O atom from the $(RhO)_{ads}$ complex. In this case, a CO_2 molecule forms, leaving behind the $CO/(Rh)_{ads}$ monocarbonyl complex. The process, Figure S10, occurs with a relatively low energy barrier, 0.45 eV, and leads to a structure where an activated CO_2 molecule is bound to the $CO/(Rh)_{ads}$ complex; from this precursor, CO_2 can desorb with an enthalpy cost of 0.63 eV. Thus, the calculations indicate that the formation of CO_2 from the reactive adsorption of the second CO molecule is a feasible process on $(RhO)_{ads}$.

Now we consider the second CO on the $(RhOH)_{ads}$ species, Figure S6c. The second CO is still strongly bound, but considerably less than the first one, suggesting two different desorption temperatures. The symmetric and antisymmetric CO stretching frequencies (2090 and 2019 cm^{-1} for terrace sites and 2096 and 2029 $cm^{-1}$for step sites) are in close agreement with experimental observation (2094 and 2031 cm^{-1}) for geminal CO; this, together with the frequencies for single CO, Table S1, 2016 cm^{-1} vs. 2010 cm^{-1} makes $(RhOH)_{ads}$ a potential candidate for the observed features.

For geminal CO molecules on $(RhO_2)_{ads}$ species, Figure S6d, the second CO is weakly bound on terrace (0.62 eV), while it is unbound (-0.07 eV) on step sites. As a result, the symmetric and antisymmetric CO stretching frequencies are blue-shifted or slightly redshifted, +16, -48 cm^{-1} for terrace sites, and -14, -45 cm^{-1} for step sites, Table S2. These two bands are completely different from those observed experimentally (see below). Therefore, one can rule out $(RhO_2)_{ads}$ species as a structure of single Rh atom on the TiO_2 surface.

Considering the second CO on $(Rh)_{subO2c}$ species, Figure S6e the adsorption energies are about 2 eV lower than the first CO molecule with binding energies of 0.75 eV and 1.01 eV for terrace and step sites, respectively, Table S2. However, the symmetric and antisymmetric CO stretching frequencies are largely redshifted, -88/-199 cm^{-1} and -100/-142 cm^{-1} for $(CO)_2/(Rh)_{subO2c}$ on terrace and step sites, respectively. These results are far from what seen experimentally, allowing us to dismiss $(Rh)_{subO2c}$ as potential candidate of a Rh single atom anchored on the TiO_2 surface.

Metallic Rh cluster on TiO_2 (101)

To compare the nature of isolated Rh atoms and metallic Rh clusters on TiO_2 surface, we adopted a Rh_4 cluster as a model for metallic Rh aggregates on TiO_2 surface. Note that the size of this cluster is much smaller than that observed from experiments, about 1 nanometer.[17] However, this can show qualitatively the different CO adsorption properties on cluster and isolated Rh atoms. On TiO_2 surface, the most stable structure of tetrahedral Rh_4 is with three bottom Rh atoms bound to three O_{2c} atoms with distance of 2.04-2.10 Å and the remaining Rh on the top of the triangle with Rh-Rh bond lengths of 2.32 – 2.54 Å, Figure S11a. This is in good agreement with previous DFT+U calculations.[18] The average Bader charge of each Rh atom is almost neutral (+0.13 |e|).

For CO adsorption complexes on Rh_4/TiO_2, we considered the single and geminal CO complexes as obtained on atomic Rh species, Table S3. The single CO was considered to adsorb on different Rh sites, on the topmost (Rh^0-top) or interface (Rh^0-int) sites with linear or bridge (two-fold coordinated sites) bonding mode, (Rh^0-Rh^0), Figure S11. As can be seen from Table S3, the CO molecule prefers to bind at the bridge sites with an adsorption energy of 2.89 eV, Figure S11d, stronger than the linear configuration either on the topmost Rh site (2.26 eV), Figure S11b, or at the interface Rh sites between Rh_4 and TiO_2 (101) surface (2.00 eV), Figure S11c. This is due to the fact that electron back donation from Rh_4 to CO at bridge site is higher than that at linear site. This is demonstrated by a large elongation the CO bond length to 1.195 Å compared to the linear structure (1.172 Å for CO on topmost Rh and 1.168 Å for CO at interface sites), Table S3. As a result, large redshifts are found for CO at bridge site (-326 cm^{-1}), while smaller redshifts are observed on linear structures (-159/-158 cm^{-1}).

Given that the most stable structure of CO is at the bridge site of Rh_4/TiO_2, the second CO was only considered at another bridge site, Figure S11f. A strong adsorption of the second CO was observed with an adsorption energy of 2.33 eV. The redshifts of symmetric and antisymmetric frequencies are still large, -308 and -348 cm^{-1}, respectively, Table S3. Clearly, CO adsorbed on supported metallic Rh cluster is much more strongly bound than on isolated Rh atoms (2.33 - 2.89 eV vs 1.25 - 2.42 eV); it also gives rise to much larger redshifts (more than 300 cm^{-1}) of CO frequencies.

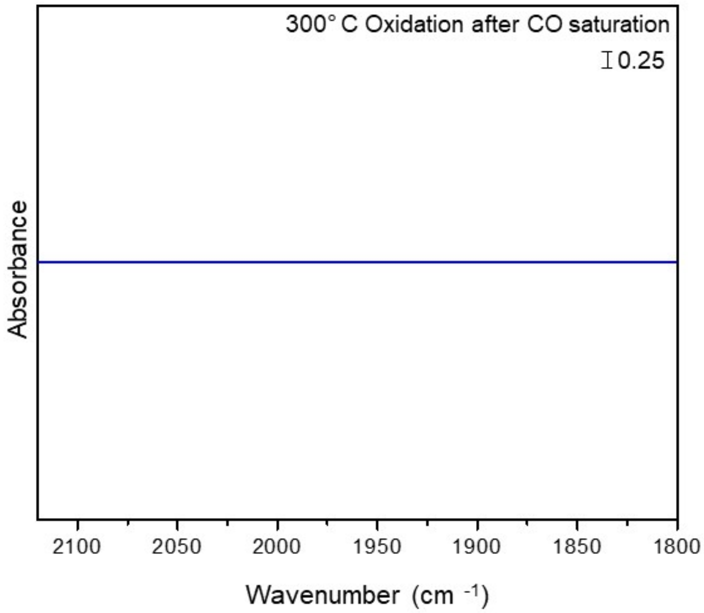

Figure S1: FTIR spectrum of Rh/TiO_2 following in-situ oxidation at 350 °C in O_2, exposure to CO at room temperature, and flushing in Ar. This shows that there is no measurable CO adsorption following oxidation pre-treatment.

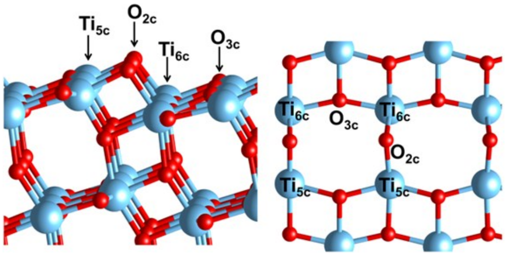

Figure S2. Side view (left) and top view (right) of TiO_2 (101) surface. The different Ti and O sites are indicated. Ti and O atoms are blue and red spheres, respectively.

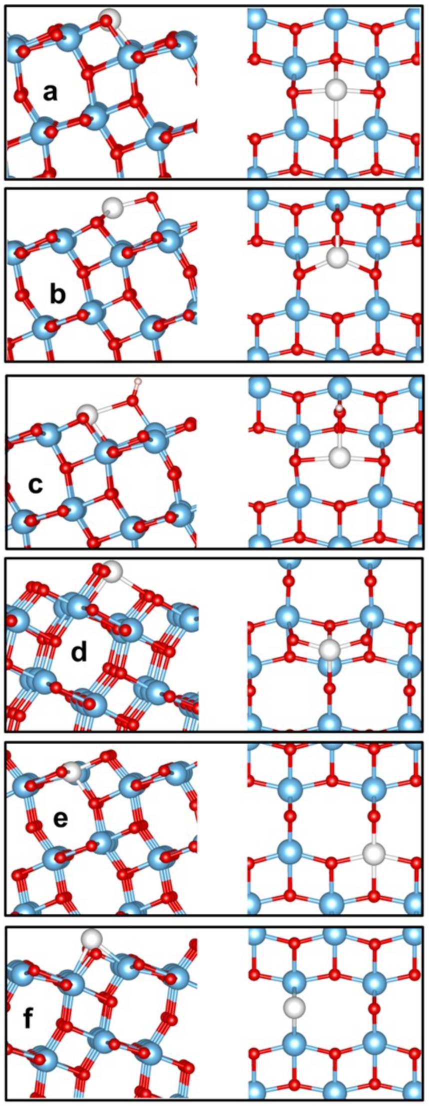

Figure S3. Side view (left) and top view (right) of isolated Rh atom on terrace sites of the TiO_2 (101) surface shown for a) $(Rh)_{ads}$, b) $(RhO)_{ads}$, c) $(RhOH)_{ads}$, d) $(RhO_2)_{ads}$, e) $(Rh)_{subTi5c}$ and f) $(Rh)_{subO2c}$. Ti, O, H and Rh atoms are blue, red, light-pink and white spheres, respectively.

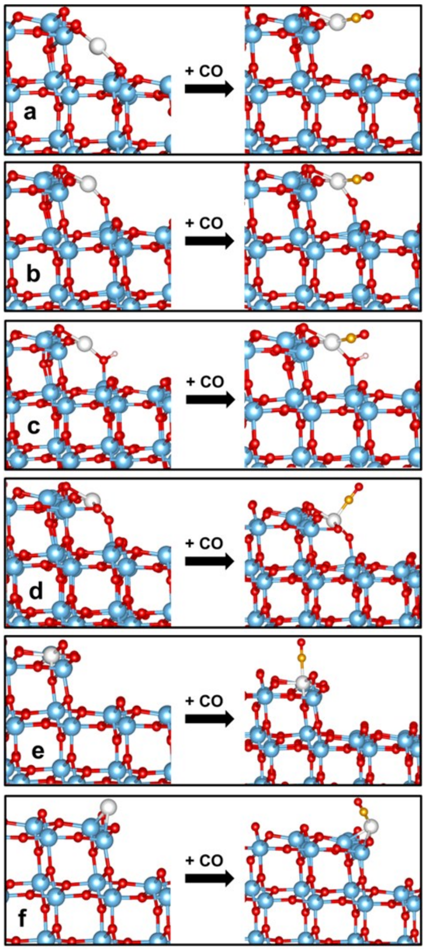

Figure S4. Rh atoms at step site (left) and the corresponding single CO adsorption complex at step site of TiO_2 (145) surface shown for a) $(Rh)_{ads}$, b) $(RhO)_{ads}$, c) $(RhOH)_{ads}$, d) $(RhO_2)_{ads}$, e) $(Rh)_{subTi5c}$, and f) $(Rh)_{subO2c}$ Ti, O, C, H and Rh atoms are blue, red, gold, light-pink and white spheres, respectively.

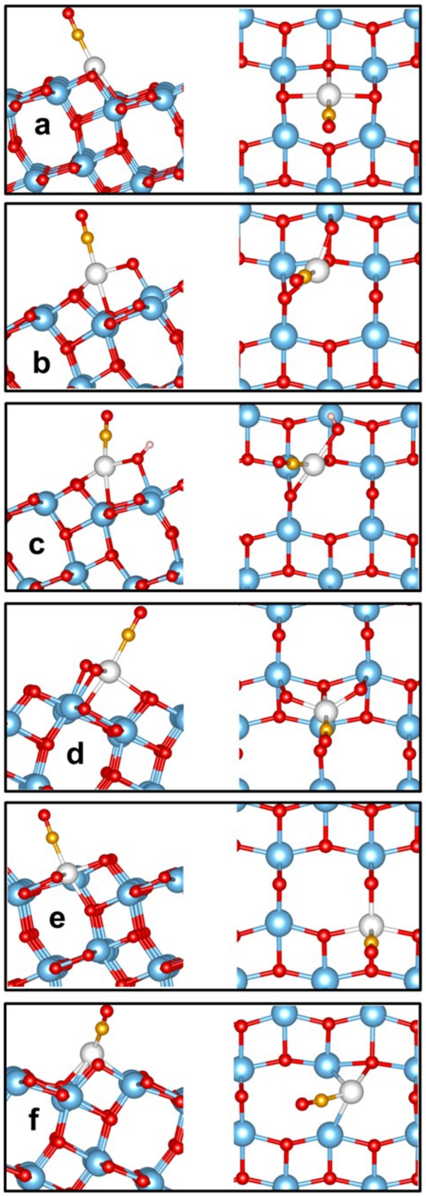

Figure S5. Side view (left) and top view (right) of single CO adsorption on a) $(Rh)_{ads}$, b) $(RhO)_{ads}$, c) $(RhOH)_{ads}$, d) $(RhO_2)_{ads}$, e) $(Rh)_{subTi5c}$ and f) $(Rh)_{subO2c}$ on anatase TiO_2 (101) surface. Ti, O, C, H and Rh atoms are blue, red, gold, light-pink and white spheres, respectively.

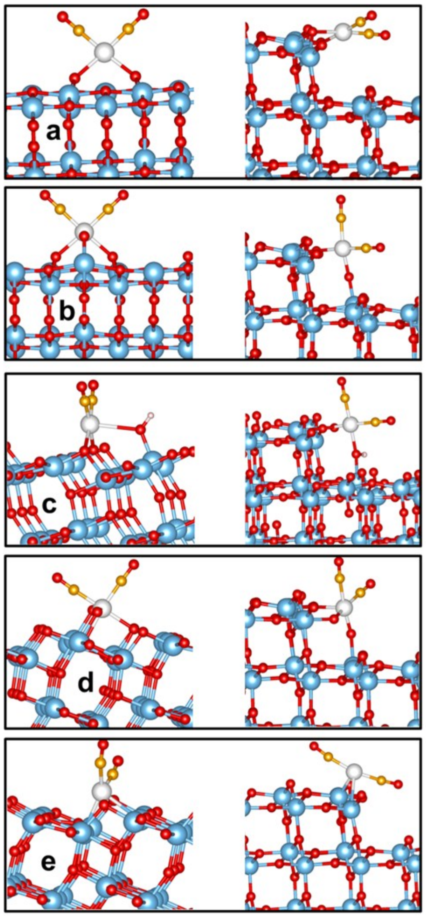

Figure S6. Geminal CO molecules on isolated Rh atoms on terrace (left) and step sites (right): a) $(Rh)_{ads}$, b) $(RhO)_{ads}$, c) $(RhOH)_{ads}$, d) $(RhO_2)_{ads}$, and e) $(Rh)_{subO2c}$. Ti, O, C, H and Rh atoms are blue, red, gold, light-pink and white spheres, respectively.

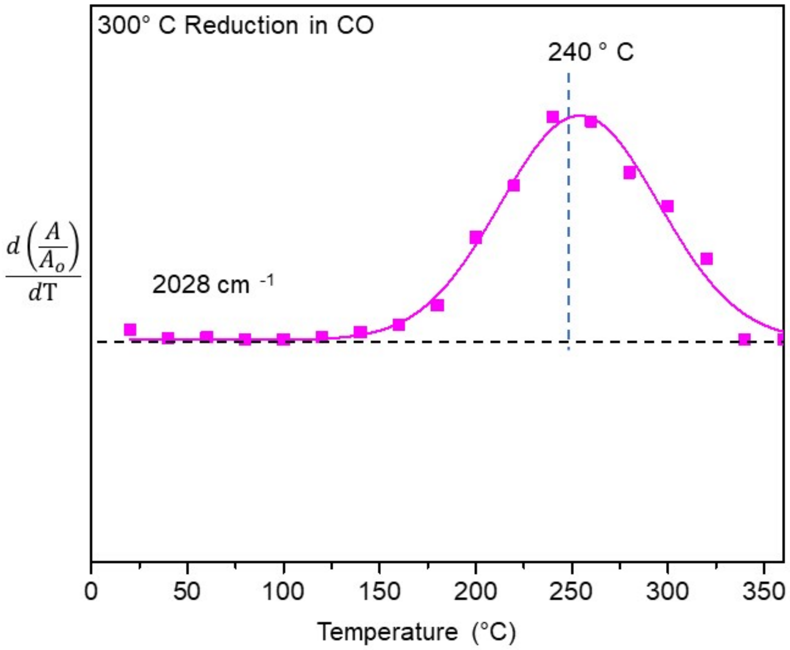

Figure S7. The rate of change of the asymmetric stretch band (2028 cm^{-1}) intensity as a function of temperature during CO TPD following 300 °C reduction in CO. The temperature where the maximum rate of loss (CO desorption) is highlighted.

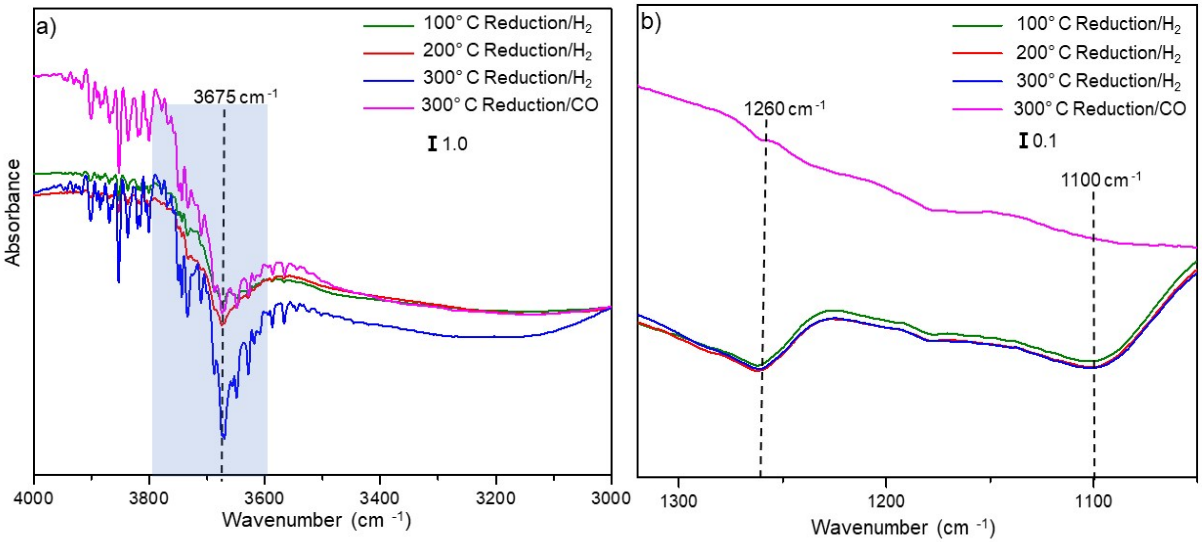

Figure S8. a) Background spectra taken at room temperature in Argon after specified reduction conditions. The highlighted region is associated with the hydroxyl species bound to TiO_2, with the intensity (negative) and peak width characterizing the density and heterogeneity, respectively. b) Background spectra taken at room temperature in Argon after specified reduction conditions. Bands at 1260 and 1100 cm^{-1} correspond to physisorbed water weakly bounded to hydroxyls at defect TiO_2 surface sites.

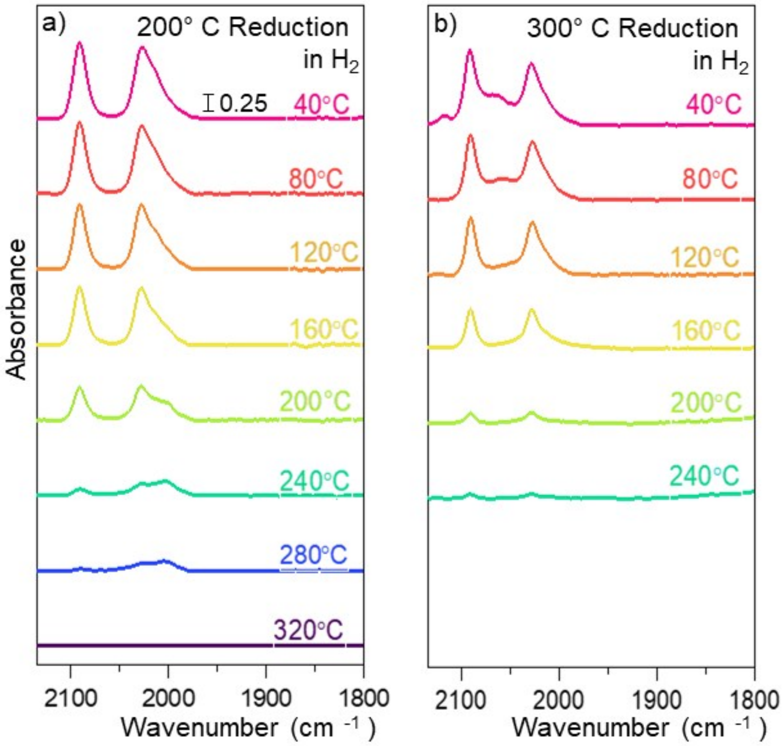

Figure S9. FTIR spectra after CO saturation and during TPD of CO from $Rh(CO)_2$ supported on anatase TiO_2 following varied pretreatment conditions : a) Reduced in H_2 at 200 °C. b) Reduced in H_2 at 300 °C.

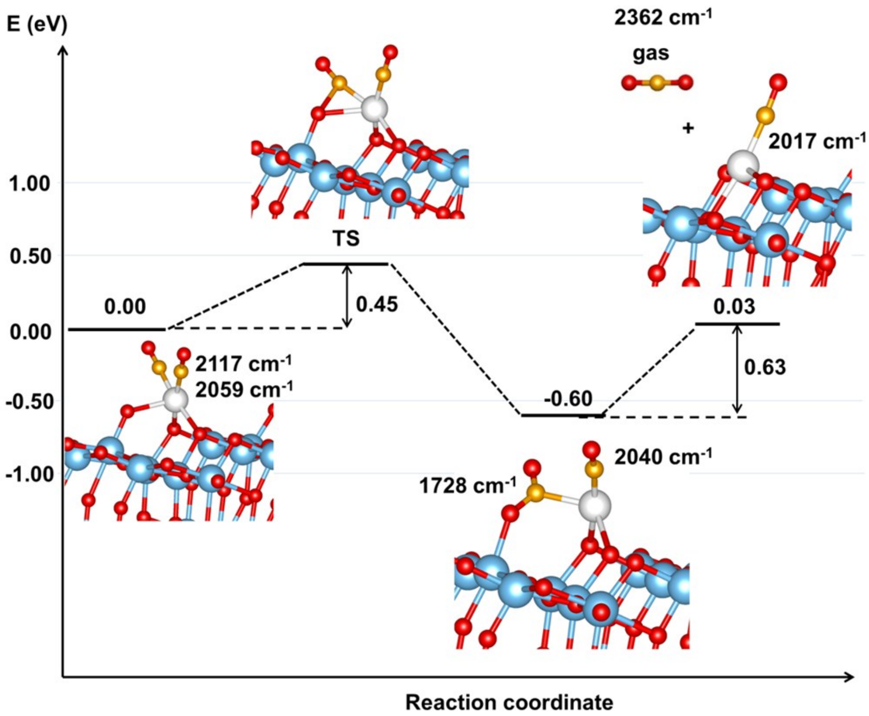

Figure S10. Reaction profile for the combination of an adsorbed CO molecule with the extra O atom of the $(RhO)_{ads}$ complex with formation and desorption of a CO_2 molecule.

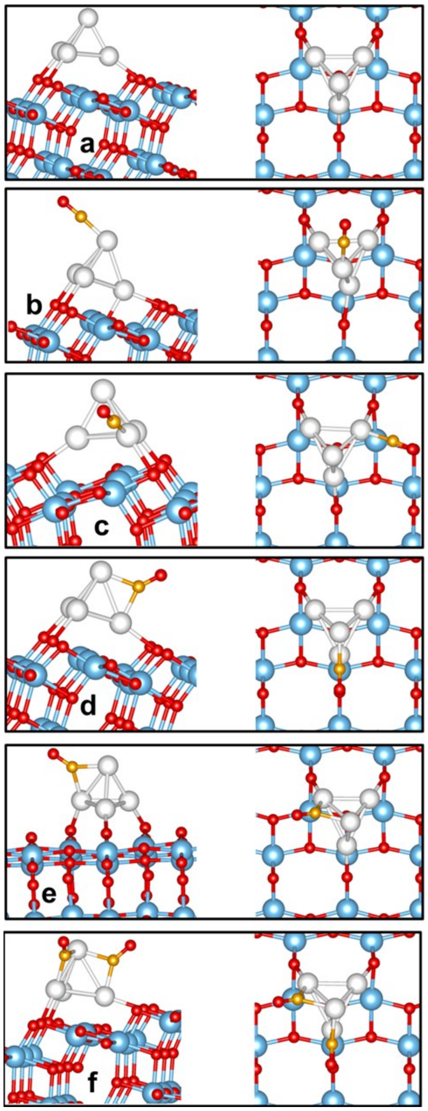

Figure S11. Side view (left) and top view (right) of a) Rh_4/TiO_2, b) mono CO adsorbed on a top Rh atom of Rh_4/TiO_2 , c) mono CO adsorbed at interface Rh site between Rh_4 and TiO_2 (101) surface, d) and e) the mono CO adsorbed bridge sites of Rh_4/TiO_2, f) the two CO molecules adsorbed at two different bridge sites of Rh_4/TiO_2. Ti, O, C and Rh atoms are blue, red, gold and white spheres, respectively.

Table S1. Adsorption energy, E_{ads} (eV), C-O bond length, R_{CO} (Å), C-Rh distance, R_{CRh} (Å), Bader charge of Rh, Q(Rh) (|e|), harmonic CO stretching frequency scaled by 2143/2125 factor, ⍰$_e$ (cm^{-1}), and frequency shift, ⍰⍰$_e$ (cm^{-1}), with respect to gas-phase CO, for CO adsorption on various single atom Rh/TiO_2 structures.

System		CO site	E_{ads} (eV)	R_{CO} (Å)	R_{CRh} (Å)	Q(Rh) (|e|)	⍰$_e$ (cm^{-1})	⍰⍰$_e$ (cm^{-1})
$(TiO_2)_{60}$[a]	Terrace	Ti^{IV}	0.34	1.138	2.467		2187	+44
$(TiO_2)_{88}$[a]	Step	Ti^{IV}	0.41	1.138	2.454		2193	+50
$(Rh)_{ads}(TiO_2)_{60}$	Terrace	Rh^0	2.05	1.166	1.813	0.64	2017	-126
$(Rh)_{ads}(TiO_2)_{88}$	Step	Rh^0	2.00	1.168	1.822	0.30	2001	-142
$(RhO)_{ads}(TiO_2)_{60}$	Terrace	Rh^I	2.24	1.160	1.828	0.97	2059	-84
$(RhO)_{ads}(TiO_2)_{88}$	Step	Rh^I	2.45	1.159	1.841	0.92	2053	-90
$(RhOH)_{ads}(TiO_2)_{60}$	Terrace	Rh^0	2.70	1.166	1.807	0.70	2016	-127
$(RhOH)_{ads}(TiO_2)_{88}$	Step	Rh^0	2.90	1.166	1.813	0.64	2016	-127
$(RhO_2)_{ads}(TiO_2)_{60}$	Terrace	Rh^{II}	1.91	1.151	1.876	1.32	2099	-44
$(RhO_2)_{ads}(TiO_2)_{88}$	Step	Rh^{II}	1.08	1.156	1.796	1.34	2091	-52
$Rh_{subTi5c}(Ti_{59}O_{120})$	Terrace	Rh^{IV}	1.58	1.149	1.863	1.45	2120	-23
$Rh_{subTi5c}(Ti_{87}O_{176})$	Step	Rh^{IV}	1.65	1.148	1.875	1.45	2117	-26
$Rh_{subO2c}(Ti_{60}O_{119})$	Terrace	Rh^{-II}	2.70	1.170	1.808	-0.02	1997	-146
$Rh_{subO2c}(Ti_{88}O_{175})$	Step	Rh^{-II}	2.56	1.170	1.811	-0.11	1993	-150

[a] Ref. 8

Table S2. Adsorption energy, E_{ads} (eV), C-O bond length, R_{CO} (Å), C-Rh distance, R_{CRh} (Å), Bader charge of Rh, Q(Rh) (|e|), harmonic CO stretching frequency scaled by 2143/2125 factor, ⍰$_e$ (cm^{-1}), and frequency shift, ⍰⍰$_e$ (cm^{-1}), with respect to gas-phase CO for geminal CO molecules adsorption on various single atom Rh/TiO_2 structures.

System		CO site	E_{ads} (eV)	R_{CO} (Å)	R_{CRh} (Å)	Q(Rh) (|e|)	⍰$_e$ (cm^{-1})[a]	⍰⍰$_e$ (cm^{-1})
$(Rh)_{ads}(TiO_2)_{60}$	Terrace	Rh^0	2.05	1.160	1.818	0.70	2097	-46
			2.03	1.160	1.828		2026	-117
$(Rh)_{ads}(TiO_2)_{88}$	Step	Rh^0	2.00	1.159	1.836	0.68	2095	-48
			1.96	1.159	1.837		2031	-112
$(RhO)_{ads}(TiO_2)_{60}$	Terrace	Rh^I	2.24	1.154	1.853	1.02	2117	-26
			1.25	1.154	1.853		2059	-84
$(RhO)_{ads}(TiO_2)_{88}$	Step	Rh^I	2.45	1.154	1.899	0.97	2108	-35
			1.08	1.153	1.863		2057	-86
$(RhOH)_{ads}(TiO_2)_{60}$	Terrace	Rh^0	2.71	1.161	1.824	0.77	2090	-53
			1.62	1.161	1.824		2019	-124
$(RhOH)_{ads}(TiO_2)_{88}$	Step	Rh^0	2.90	1.159	1.836	0.70	2096	-47
			1.66	1.160	1.831		2029	-114
$(RhO_2)_{ads}(TiO_2)_{60}$	Terrace	Rh^{II}	1.91	1.143	1.907	1.29	2159	+16
			0.62	1.151	1.874		2095	-48
$(RhO_2)_{ads}(TiO_2)_{88}$	Step	Rh^{II}	1.08	1.145	2.009	1.24	2129	-14
			-0.07	1.147	1.972		2098	-45
$Rh_{subO2c}(Ti_{60}O_{119})$	Terrace	Rh^{-II}	2.70	1.155	1.990	0.03	2055	-88
			0.75	1.168	1.817		1994	-149
$Rh_{subO2c}(Ti_{88}O_{175})$	Step	Rh^{-II}	2.56	1.159	1.907	-0.17	2043	-100
			1.01	1.159	1.919		2001	-142

Table S3. Adsorption energy, E_{ads} (eV), C-O bond length, R_{CO} (Å), C-Rh distance, R_{CRh} (Å), Bader charge of Rh bound to CO, Q(Rh) (|e|), harmonic CO stretching frequency scaled by 2143/2125 factor, ⍰$_e$ (cm^{-1}), and frequency shift ⍰⍰$_e$ (cm^{-1}) with respect to gas-phase for CO adsorption on Rh_4/TiO_2 structures.

System	CO site	E_{ads} (eV)	R_{CO} (Å)	R_{CRh} (Å)	Q(Rh) (|e|)	⍰$_e$ (cm^{-1})	⍰⍰$_e$ (cm^{-1})
$(CO)Rh_4(TiO_2)_{60}$	Rh^0-top	2.26	1.172	1.800	0.19	1984	-159
$(CO)Rh_4(TiO_2)_{60}$	Rh^0-int	2.00	1.168	1.843	0.25	1985	-158
$(CO)Rh_4(TiO_2)_{60}$	Rh^0-Rh^0	2.89	1.195	1.930, 1.937	0.15	1817	-326
$(CO)_2Rh_4(TiO_2)_{60}$	Rh^0-Rh^0	2.89	1.197	1.958, 1.927	0.23	1835	-308
		2.33	1.196	1.916, 1.969		1795	-348

References

---

(1) Redhead, P.A. Thermal desorption of gases. Vacuum **1996**, *12* (4), 203-211.

(2) Perdew, J. P.; Burke, K.; Ernzerhof, M. Generalized Gradient Approximation Made Simple. *Phys. Rev. Lett.* **1996**, *77* (18), 3865-3868.

(3) Kresse, G.; Furthmüller, J. Efficiency of Ab-Initio Total Energy Calculations for Metals and Semiconductors Using a Plane-wave Basis Set. *J. Comput. Mater. Sci.* **1996**, *6* (1), 15-50.

(4) Anisimov, V. I.; Zaanen, J.; Andersen, O. K. Band Theory and Mott Insulators: Hubbard U Instead of Stoner I. *Phys. Rev. B* **1991**, *44* (3), 943-954.

(5) Dudarev, S. L.; Botton, G. A.; Savrasov, S. Y.; Humphreys, C. J.; Sutton, A. P. Electron-Energy-Loss Spectra and the Structural Stability of Nickel Oxide: An LSDA+U Study. *Phys. Rev. B* **1998**, *57* (3), 1505-1509.

(6) Chen, H.Y.T.; Tosoni, S.; Pacchioni, G. Adsorption of Ruthenium Atoms and Clusters on Anatase TiO_2 and Tetragonal ZrO_2 Surfaces: A Comparative DFT Study. *J. Phys. Chem. C* **2015**, *119* (20), 10856-10868.

(7) Blöchl, P.E. Projector Augmented-Wave Method. *Phys. Rev. B* **1994**, *50* (24), 17953.

(8) Kresse, G.; Joubert, J. From Ultrasoft Pseudopotentials to the Projector Augmented-Wave Method. *Phys. Rev. B* **1999**, *59* (3), 1758.

(9) Chen, H.-Y.T.; Tosoni, S.; Pacchioni, G. A DFT Study of the Acid-Based Properties of Anatase TiO_2 and Tetragonal ZrO_2 by Adsorption of CO and CO_2 Probe Molecules. *Surf. Sci.* **2016**, 652, 163-171.

(10) P. Janthon, F. Viñes, J. Sirijaraensre, J. Limtrakul, and F. Illas. Adding Pieces to the CO/Pt(111) Puzzle: The Role of Dispersion. J. Phys. Chem. C 2017, 121, 3970–3977

(11) Tang, W.; Sanville, E.; Henkelman, G. A Grid-Based Bader Analysis Algorithm without Lattice Bias. *J. Phys.: Condens. Matter.* **2009**, *21* (8), 084204.

(12) Sanville, E.; Kenny, S. D.; Smith, R.; Henkelman, G. An Improved Grid-Based Algorithm for Bader Charge Allocation. *J. Comp. Chem.* **2007**, *28* (5), 899-908.

(13) Henkelman, G.; Arnaldsson, A.; Jónsson, H. A Fast and Robust Algorithm for Bader Decomposition of Charge Density. *Comput. Mater. Sci.* **2006**, *36* (3), 254-360.

(14) Yu, M.; Trinkle, D. R. Accurate and Efficient Algorithm for Bader Charge Integration. *J. Chem. Phys.* **2011**, *134* (6), 064111.

(15) Henkelman, G.; Jonsson, H. Improved Tangent Estimate in the Nudged Elastic Band Method for Finding Minimum Energy Paths and Saddle Points. *J. Chem. Phys.* **2000**, *113* (22), 9978-9986.

(16) Thang, H. V.; Pacchioni, G.; DeRita, L.; Christopher, P. Nature of Stable Atom Pt Catalysts Dispersed on Anatase TiO_2. *J. Catalysis* **2018**, *367*, 104-114.

(17) Matsubu, J. C.; Yang, V. N.; Christopher, P. Isolated Metal Active Site Concentration and Stability Control Catalytic CO_2 Reduction Selectivity. *J. Am. Chem. Soc.* **2015**, *137* (8), 3076-3084.

(18) Guo, D.; Wang, G.-C. Partial Oxidation of Methane on Anatase and Rutile Defective TiO_2 Supported Rh_4 Cluster: A Density Functional Theory Study. *J. Phys. Chem. C* **2017**, *121* (47), 26308-236320.